On Determining the Sign of Fault Vectors by X-Ray Topography

A. R. LANG

H. H. Wills Physics Laboratory, University of Bristol, England

(Z. Naturforsch. **27 a**, 461—468 [1972]; received 13 December 1971)

Dedicated to Prof. Dr. K. MOLIÈRE *on his 60-th birthday*

Experiments show that the excess or deficiency of diffracted intensity in the image of the first fringe in stacking-fault-type fringe patterns on X-ray projection topographs can give a clear indication of the sign of the fault vector even when μt is no greater than unity (μ is the normal linear absorption coefficient and t is the crystal thickness) provided that the crystal structure is such as will exhibit fairly strong anomalous transmission (Borrmann effect) in the thick crystal case for the Bragg reflections used. A quite simple diffraction theory suffices to account for the observations. Sign determinations based on this theory agree with those expected at Brazil twin boundaries parallel to major rhombohedral planes in quartz.

1. Introduction

It is not very difficult to find transmission electron micrographs of lattice defects such as dislocations, precipitates and stacking faults which when printed with an overall magnification of, say, 50,000, look so like X-ray projection topographs [1] of similar crystal defects reproduced at a magnification of about 100 that an experienced eye is needed to distinguish between them provided that their grossly different magnifications are not disclosed. Nevertheless, it is accepted that to explain adequately the X-ray diffraction contrast caused by lattice defects a theoretical treatment rather different from that employed in the electron case is required. Some of the necessary differences in the diffraction contrast theories arise from obvious differences in the experimental parameters. For example, the larger Bragg angles, specimen thicknesses and extinction distances applying in the X-ray case combine to render inapplicable the "column approximation" which has so greatly facilitated diffraction contrast calculations in transmission electron microscopy. On the other hand, "two-beam" theory will apply to all parts of X-ray topograph images except where quite locally, and generally quite fortuitously, the stringent conditions for nonsystematic simultaneous reflections are satisfied. There are other differences of more subtle nature between the electron and X-ray diffraction theories applicable under usual experimental conditions. Perhaps the most interesting difference is the need for a spherical-wave dynamical diffraction theory in the X-ray case. Kato first pointed out that plane-wave dynamical diffraction theory was not adequate for explaining the Pendellösung fringe phenomena observed on X-ray section topographs [2]; the appropriate spherical-wave theory was developed by him [3], and he has presented an instructive comparison of the wave-optical conditions operating in X-ray and electron diffraction cases [4].

Lacking the simplification of one-dimensional calculation that the column approximation brings, and perforce carrying the burden of integration over all values of deviation parameter, diffraction contrast calculations relating to images of lattice imperfections on X-ray projection topographs are generally of formidable complexity. It is the theme of this paper to show that the absence of complete theory need not necessarily impede the interpretation of X-ray projection topographs. On the contrary, the simplest diffraction theory can occasionally be invoked to explain leading features of the observed X-ray diffraction contrast. The analysis may take the form of an adaptation for X-rays of a special case treated in electron microscope theory. Pursuing the analogy with electron diffraction can thus lead fruitfully to the extraction of wanted data concerning certain lattice defects, provided due consideration be given to the reasonableness of applying highly simplified analyses to the experimental situation under examination. This approach will be illustrated by the determination of the sign of the fault vector at the fault surface produced by a Brazil twin boundary in alpha quartz.

Reprint requests to Dr. A. R. LANG, H. H. Wills Physics Laboratory, University of Bristol, Tyndall Avenue, Royal Fort, *Bristol BS 8 ITL*, England.

2. Fault Surfaces

Techniques for the direct imaging of lattice defects have revealed the existence of many types of fault surface. In electron microscopy, theory is extensive and observations profuse: both have been comprehensively reviewed [5, 6]. In X-ray topography some accounts of observations have been put on record [7, 8]; but theory has been developed up to now only for certain of the simpler situations. A fault surface is an interface separating two domains in the crystal. The relationship between the domains can take various descriptions of which the two simplest are, firstly, that the Bravais lattice of one domain is translated relative to that of the other by a constant *fault vector*, $\boldsymbol{f}$, and, secondly, that the displacement of a lattice point in one domain relative to what would have been the corresponding lattice point in the perfect crystal with no fault surface is a linear function of distance from the fault surface. In the terminology of GEVERS, VAN LANDUYT and AMELINCKX [9] the former type of fault is an α-boundary, giving rise to α-fringes in its diffraction contrast image, whereas the latter type is a δ-boundary and its fringes are δ-fringes. Important examples of δ-boundaries are 90° Bloch walls in ferromagnetic single crystals [8], and the classic example of the α-boundary is the stacking fault. Interesting examples of α-boundaries are those twin boundaries across which lattice *parallelism* is maintained but lattice *coincidence* is not. Twinning of this lattice-parallel type is a possibility when the crystal structure has a lower symmetry than that of its Bravais lattice: the twin law may be a symmetry operation corresponding to a symmetry element which is possessed by the Bravais lattice but is absent in the structure of the crystal. The actual structure and width of the transition region between domains may be a subject worthy of investigation. From the diffraction point of view, however, the width of the transition region is immaterial provided it is but a small fraction of the extinction distance. In the X-ray case when extinction distances are typically a few tens of microns, lattice-parallel twin boundaries in quartz in which the transition region is effectively one unit cell in thickness, and 90° Bloch wall boundaries in iron-silicon alloy which are of order 10^3 Å in thickness, behave equally as ideal, single interfaces. It follows that X-ray topography can provide no direct information concerning the crystal structure in the boundary region. It can only establish the fault vector $\boldsymbol{f}$; but this it can do quite accurately, both in magnitude and sign.

From the diffraction contrast produced by the fault surface in the Bragg reflection whose diffraction vector is $\boldsymbol{g}$ (g is the reciprocal of the interplanar spacing) one can assess the value of the phase angle α where $\alpha = (2\pi \boldsymbol{g}\cdot\boldsymbol{f})$ modulo 2π. Reflections diagnostically valuable for finding $|\boldsymbol{f}|$ are those for which $\boldsymbol{g}\cdot\boldsymbol{f}$ is zero or an integer, in which cases the fault becomes invisible. The ease with which many different reflections up to fairly high orders can be examined separately under strict two-beam conditions in X-ray topography makes possible the precise determination of $|\boldsymbol{f}|$ by this technique. At stacking faults in the face-centred cubic metals α is restricted to the values 0 and $\pm 2\pi/3$. In the diamond and blende structures it is assumed that values of α are similarly restricted, and this appears to be true within close limits. However, it is known that the spacings between one zinc-sulphur double-layer and the next are about 0.1% different in the 3 C stacking sequence (blende) and the 2 H sequence (wurtzite). In X-ray topographs of highly perfect ZnS polytypes there is diffraction-contrast evidence for a change in mean interlayer spacing when there is a change in the relative amounts of cubic and hexagonal stacking [10]. This implies that stacking fault vectors in, say, blende possess a very small component normal to the stacking-fault plane. It is worth considering whether X-ray topography may have sufficient sensitivity to detect small components of stacking-fault vectors normal to the planes of individual stacking faults in the less simple structures. Such components are, of course, absent in simple sphere-stacking models. In the case of lattice-parallel twin boundaries in the general case, there is no prior prescription, by reference to known translation vectors, of expected discrete values of $\boldsymbol{f}$. The magnitude, direction and sense of $\boldsymbol{f}$ must all be found by experiment, and a plausible crystal-structural model for the twin-boundary structure must be devised that will agree with the experimentally determined value of $\boldsymbol{f}$.

KATO, USAMI and KATAGAWA [11] calculated from spherical-wave dynamical diffraction theory the pattern of fault fringes that should appear on a section topograph of a non-X-ray absorbing crystal, the fault-fringes being caused by interbranch scattering

at an α-boundary. The mean intensity of the fault-fringe pattern is proportional to $\sin^2(\frac{1}{2}\alpha)$. Obviously the fringes are most strongly visible when $|\boldsymbol{g}\cdot\boldsymbol{f}| = \frac{1}{2}$, but the contrast in the zero-absorption case is independent of the sign of α in its range $-\pi \leqq \alpha \leqq \pi$. AUTHIER [12] extended previous fault-fringe calculations by himself and SAUVAGE [13], which included absorption, to derive expressions for the fault fringe pattern produced by boundaries with similar geometry to those discussed by KATO et al. [11] but applicable to the case of thick, highly absorbing crystals. Authier discussed the contrast of the first fringe that appears at the image of the outcrop of the stacking fault at either X-ray entrance or exit faces of a parallel-sided specimen. His expression includes a term proprotional to $\sin\alpha$, and he concluded correctly that in the diffracted-beam section topograph the sense of contrast (i. e. excess or deficiency of intensity compared with the unfaulted crystal) depends upon the sign of α, and that for a given α it will be opposite for outcrops at the exit and entrance surfaces. Earlier experiments by the present author had shown that on projection topographs the sign of α can be found from the excess or deficiency in the contrast of the first fringe, at any rate at its outcrop on the X-ray exit surface, in the case of strong reflections from quartz even when μt was no greater than about unity (μ is the normal linear absorption coefficient and t the thickness of the specimen plate). It is useful to know that the sign of fault vectors can be determined from X-ray projection topographs without the need for making μt large, for one then retains the advantages of taking topographs under conditions of no more than moderate absorption. These advantages include shorter exposure times, good visibility of dislocations, reasonably sharp imaging of defects near the X-ray entrance surface as well as near the exit surface with consequent ease in interpretation of the three-dimensional configuration of defects.

3. Observations on Quartz

Figure 1 is a stereographic projection parallel to the c-axis of quartz showing poles of planes whose Bragg reflections produce useful X-ray topographs. The three major rhombohedral faces of form r $\{10\bar{1}1\}$ whose indices are $(10\bar{1}1)$, $(\bar{1}101)$ and $(0\bar{1}11)$, together with the three minor rhombohedra z $\{01\bar{1}1\}$ whose indices are $(01\bar{1}1)$, $(\bar{1}011)$ and $(1\bar{1}01)$ make

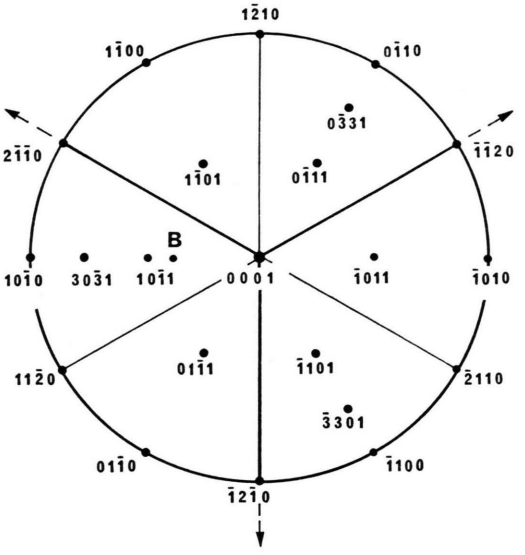

Fig. 1. Stereographic projection parallel to c-axis of quartz: B is pole of plane of the BT-cut plate.

up the cap that terminates the typical finger-like habit which is sketched in Figure 2. The small faces s $\{11\bar{2}1\}$ and x $\{51\bar{6}1\}$ from which the morphological hand may be determined are omitted from the simplified drawing, Figure 2. Consequently, this sketch represents equally well laevo-rotatory quartz which is structurally right-handed, space group $P3_12$, or its enantiomorph whose space group is $P3_22$. (It is in any case rare that these small faces

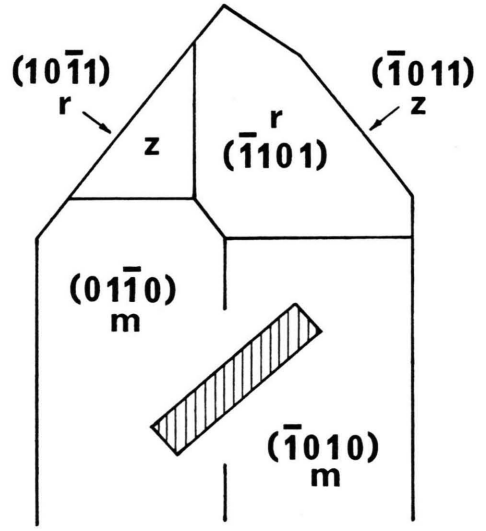

Fig. 2. Idealised drawing of quartz crystal bounded by prism $m\{10\bar{1}0\}$ and capped by $r\{10\bar{1}1\}$ and $z\{01\bar{1}1\}$. Axis $\boldsymbol{a}_2$ of Fig. 1 points towards observer. Shaded rectangle represents BT plate in correct orientation relative to natural faces.

are as nicely developed as the drawings in mineralogical texts portray.) The Brazil twin law, which changes the chirality by a reflection across $\{11\bar{2}0\}$, maintains lattice parallelism but introduces an α-boundary at the twin composition surface. Brazil twins can be distinguished X-ray topographically by reflection intensity differences caused by anomalous dispersion when certain Bragg planes not belonging to the zones of the two-fold rotation symmetry axes parallel to the lattice vectors $\boldsymbol{a}_1$, $\boldsymbol{a}_2$, and $\boldsymbol{a}_3$ are used [14]. On the other hand, when Friedel's Law is obeyed, the X-ray topographic detection of Brazil twinning depends upon recognizing the particular characteristics of Brazil twin boundary fault surfaces by which they may be identified in comparison with other types of fault surface that may be present. Typically, Brazil twin boundaries run straight and smooth (within X-ray topographic resolution limits) over areas up to centimetres square in extent. They have a preference for orientations parallel to the forms $r\{10\bar{1}1\}$, $z\{01\bar{1}1\}$ and $m\{10\bar{1}0\}$. Twin boundary fault surfaces parallel to each form have characteristic X-ray topographic visibility rules because the twin-boundary structure, and hence $\boldsymbol{f}$, depends upon the orientation of the composition plane.

Figures 3 a and b show X-ray topographs of part of a quartz plate, thickness 1 mm, which was cut in the BT oscillator-plate orientation but which had to be rejected because it contained a wedge-shaped insert of Brazil-twinned material. This wedge spreads out from a point near the upper left corner of the field of Figure 3 *. At this point there is a strain-producing body, probably an inclusion, which apparently caused the twin to nucleate. It also generated a diverging bundle of dislocations some of which run parallel to the twin boundaries. These dislocations, and also other dislocations located in the bottom and lower right-hand parts of the field, exhibit strong positive contrast (i. e. excess difracted intensity compared with the more perfect crystal matrix surrounding them) under the conditions of fairly low absorption obtaining. (The topographs in Figs. 3 and 4 are positive prints, hence extra blackness represents extra diffracted intensity, i. e. blackness, on the original topograph emulsions.) The strain fields associated with growth layering, which have much weaker strain gradients than those close to dislocation lines, produce contrast mainly as a consequence of "energy-flow curvature" without interbranch scattering [15]. Consequently, in the presence of moderate absorption, their images tend to show a reversal of contrast in the $h\,k\,l$ and $\bar{h}\,\bar{k}\,\bar{l}$ reflections. These growth layers are seen as the set of parallel diffuse light or dark bands running in the direction of the top-right to bottom-left diagonal of the field. They are parallel to traces of $(\bar{1}101)$ planes, since this region of the specimen is comprised of material that crystallized on the $(\bar{1}101)$ face. The direction of growth thus points from upper left to lower right in Fig. 3: the wedge of twinned crystal widens out in this direction, and the dislocation bundles (some of which are obviously generated at inclusions) also fan out in directions making fairly small angles with the perpendicular to the growing crystal face. [In the whole crystal slice of which Figs. 3 and 4 show only a part, growth sectors other than $(\bar{1}101)$ are represented: their growth banding, and fault surface fringes at boundaries between growth sectors, have been illustrated in an earlier account of imperfections in this crystal. [7]]

The geometry of the twin-boundary images as they appear in Figs. 3 and 4 can be understood by reference to Figs. 1 and 2. Of chief concern here is the twin boundary that lies parallel to $(10\bar{1}1)$. This boundary makes $10\frac{3}{4}^\circ$ with the plane of the BT cut. It generates the vertical, broad, fault surface fringes covering the triangular area extending from the apex of the twin wedge in the upper left corner of the field to the vertical line parallel to $\boldsymbol{a}_2$ along which the twin boundary outcrops at the specimen surface. In both Figs. 3 and 4 the outcrop is on the X-ray *exit* face of the specimen. Thus, referring to Fig. 2, the incident X-ray beam impinges on the lower face of the BT plate, whilst the upper face of the plate is nearer to the photographic emulsion that records the topograph.

When $\boldsymbol{g}\cdot\boldsymbol{f}$ is non-zero, the mean contrast of the twin boundaries, taking an average both over the intensity oscillations of the fringes and over $h\,k\,l$, $\bar{h}\,\bar{k}\,\bar{l}$ pairs, is positive with the $\mu\,t$ values applying to this specimen thickness when using MoKα or AgKα radiations. With MoKα, as used in the topographs of Figs. 3 and 4, the contrast of the first fringe in the twin-boundary fault fringe pattern is generally opposite in $h\,k\,l$, $\bar{h}\,\bar{k}\,\bar{l}$ pairs of topograph images. The geometrical conditions which render this contrast reversal strongly manifest include those

* Figures 3 and 4 on page 464 a.

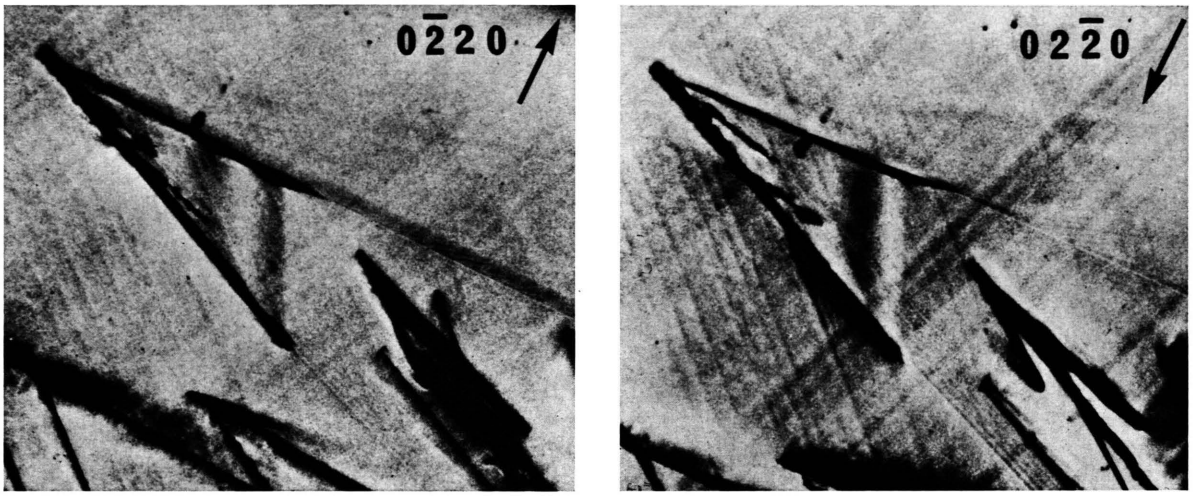

Fig. 3. X-ray topographs of part of BT-cut plate 1 mm thick. The wedge-shaped Brazil-twinned portion is bounded by planes $(01\bar{1}0)$ and $(0\bar{1}11)$ steeply inclined to the specimen surface and by a triangular segment of $(10\bar{1}1)$ which outcrops at the X-ray exit surface of the specimen. Fault vector $\boldsymbol{f}$ and axis $\boldsymbol{a}_2$ are directed vertically downwards. Arrows, length $\frac{3}{4}$ mm, are projections of diffraction vector, $\boldsymbol{g}$, which makes 19° with specimen surface. Parallax causes change in relative positions of dislocation images in this $h\,k\,l$, $\bar{h}\,\bar{k}\,\bar{l}$ stereo-pair. Radiation MoKα_1. (a) Reflection $0\bar{2}20$; $\boldsymbol{g}\cdot\boldsymbol{f}=+0.12$ predicted from twin-boundary structure model, and the first fringe shows positive contrast (i. e. excess intensity); (b) reflection $02\bar{2}0$; predicted $\boldsymbol{g}\cdot\boldsymbol{f}=-0.12$, first fringe shows negative contrast.

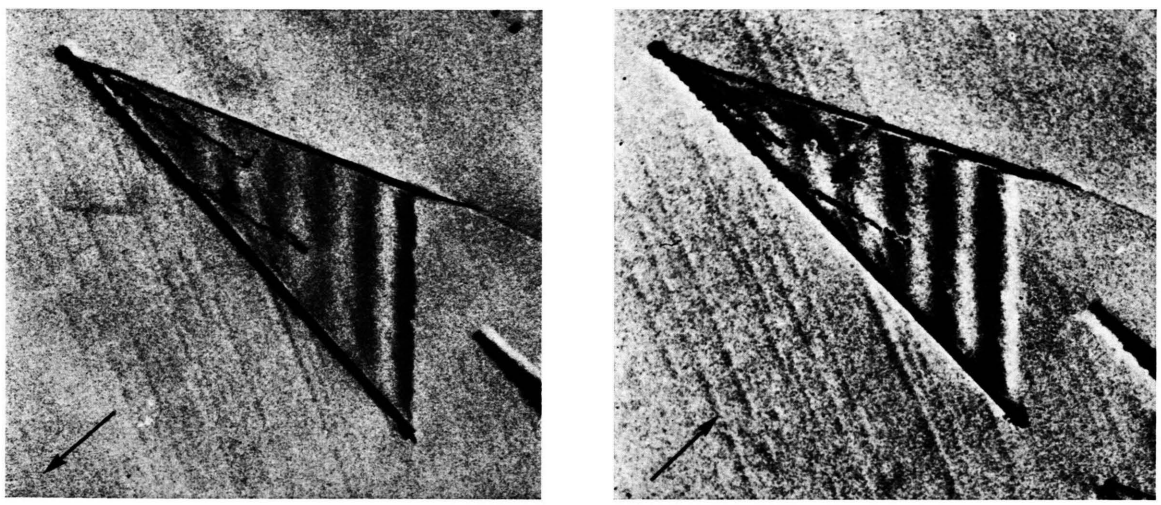

Fig. 4. Stereo-pair of $01\bar{1}\bar{1}$ and $0\bar{1}11$ reflections, MoKα_1 radiation. Arrows, length $\frac{1}{2}$ mm, are projections of $\boldsymbol{g}$ which is inclined 11° to the specimen surface. (a) Reflection $01\bar{1}\bar{1}$; predicted $\boldsymbol{g}\cdot\boldsymbol{f}=+0.11$, positive contrast in first fringe. (b) Reflection $0\bar{1}11$; predicted $\boldsymbol{g}\cdot\boldsymbol{f}=-0.11$, negative contrast in first fringe.

obtaining in Figs. 3 and 4: i. e., the twin boundary outcrops on the X-ray exit face of the specimen, it makes a fairly small angle with the specimen face, and the diffraction geometry does not depart greatly from the symmetrical Laue case.

4. Simplified Theory

Assumptions

Figure 5 represents a cross-section of a parallel-sided crystal plate which is perfect except for division into domains I and II by a fault surface cutting through the specimen from outcrop P on the X-ray entrance surface to outcrop Q on the X-ray exit surface. The fault vector $\boldsymbol{f}$ is defined as the translation

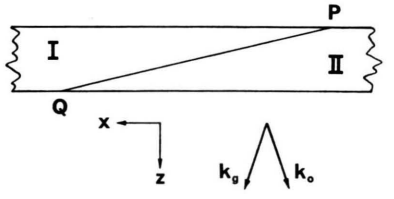

Fig. 5. Diagrammatic section in the plane of incident and diffracted X-rays showing trace of a fault surface transecting the crystal plate from P on the X-ray entrance face to Q on the X-ray exit face. X-rays pass from domain I to domain II.

of domain II with respect to domain I. The incident and diffracted X-rays lie in the plane of the diagram. The discussion following will be concerned with their wave vectors in the crystal, which are related by $\boldsymbol{k}_g^{(i)} = \boldsymbol{k}_0^{(i)} + \boldsymbol{g}$, where the superscript i is 1 or 2 for waves associated with the correspondingly-numbered branches of the dispersion surface. In the lower part of Fig. 5 the orientation of $\boldsymbol{k}_0$ and $\boldsymbol{k}_g$ relative to orthogonal axes $0x$ and $0z$ is indicated: $\boldsymbol{g}$ is parallel to the positive x direction. The analysis simply consists of matching waves in I and II to ensure continuity of wave-disturbance across the fault surface; and the physical arguments regarding the effects of absorption are well known in transmission electron microscopy [16]. The assumptions are:

(i) $\boldsymbol{g}$ makes a sufficiently small angle with the trace of the fault surface in Fig. 5 that the spatial variation of wave-disturbance along the trace may be expressed in terms of variation of the coordinate x only, for the purpose of matching waves across the fault surface. Also, the angle made by PQ with the X-ray exit and entrance surfaces of the specimen is small enough that the coordinate z serves equally well as a measure of distance normal to the entrance surface as it does of distances normal to PQ and parallel to the Bragg plane.

(ii) Only waves exactly satisfying the Bragg condition in the crystal are considered. These dominate in forming the fault-fringe pattern on a projection topograph taken under the geometrical conditions specified in (i) above.

(iii) Absorption is appreciable, and the structure produces a sufficiently strong Borrmann effect to render branch (1) waves exactly satisfying the Bragg condition dominant after passing through the whole thickness of the crystal. This thickness is assumed to be many times greater than the Pendellösung period. X-ray topographic manifestations of the Borrmann effect become significant when $\mu t \geqq 1$ and the ratio $\varepsilon = F_g''/F_0''$ is greater than $\sim \frac{1}{2}$. [The g-th Fourier coefficient of the electron-density distribution is referred to an origin placed on a symmetry plane of this Fourier component so that when writing F_g as the sum of a real part F_g' and an imaginary part F_g'' the latter represents absorption only. Also, that symmetry plane is chosen which makes F_g' positive. F_0'' and μ are related by $\mu = (2\lambda r_e/V)\, F_0''$, where r_e is the classical electron radius and V is the unit cell volume; and it is assumed for simplicity that F_g'' is positive and equal to F_{-g}''.]

Fault Surface Outcrop at Exit Surface

In the crystal, under assumption (ii), the x-components of $\boldsymbol{k}_g^{(i)}$ are $\frac{1}{2}g$, and those of $\boldsymbol{k}_0^{(i)}$ are $-\frac{1}{2}g$. Denoting the z-components of $\boldsymbol{k}_0^{(2)}$ and $\boldsymbol{k}_g^{(2)}$ by k_z, then the z-components of $\boldsymbol{k}_0^{(1)}$ and $\boldsymbol{k}_g^{(1)}$ are $(k_z + D)$ where D^{-1} is the Pendellösung period measured along the Bragg planes. Consider a region of the fault surface near Q. Then, on the domain I side of the fault surface, the variation with x of the wave-disturbance may be written simply as

$$\exp(-\pi i g x) - \exp(\pi i g x), \qquad (1)$$

the first term being contributed by the $k_0^{(1)}$ wave and the second by the $k_g^{(1)}$ wave, for, following assumption (iii), branch (2) waves are neglected in comparison with branch (1) waves. (The origin of x is placed on the same symmetry plane of the g-th Fourier component of electron density as was chosen to make F_g' positive.) Suppose the x-component of the fault vector $\boldsymbol{f}$ is f_x. Then at the fault surface a

point x in I comes opposite a point in II whose coordinate is x' with respect to the equivalent origin in II, and $x' = x - f_x$. The disturbance, expression (1), is continuous across the fault surface, and on the domain II side must be written as

$$\exp(-\pi i g x') \exp(-i\alpha/2) - \exp(-\pi i g x') \exp(i\alpha/2), \quad (2)$$

where $\alpha = 2\pi \boldsymbol{g}\cdot\boldsymbol{f}$. Expression (2) can be identified with the sum of branch (1) and branch (2) Bloch waves in domain II,

$$\psi^{(1)}[\exp(-\pi i g x') - \exp(\pi i g x')] + \psi^{(2)}[\exp(-\pi i g x') + \exp(\pi i g x')]. \quad (3)$$

The identity of (2) and (3) gives

$$\psi^{(1)} = \cos(\tfrac{1}{2}\alpha) \text{ and } \psi^{(2)} = -i\sin(\tfrac{1}{2}\alpha). \quad (4)$$

Now consider how the $k_0{}^{(i)}$ and $k_g{}^{(i)}$ waves propagate in domain II. If the exit surface is at a sufficiently small distance z below the fault surface that the difference in attenuations of the branch (1) and branch (2) waves can be neglected, then the resultant incident-direction wave (0-wave) at the exit surface is

$$\exp(-\pi i g x') \exp(2\pi i k_z z) \cdot [\psi^{(1)} \exp(2\pi i D z) + \psi^{(2)}], \quad (5)$$

and the resultant diffracted-direction wave (G-wave) is

$$\exp(\pi i g x') \exp(2\pi i k_z z) \cdot [\psi^{(2)} - \psi^{(1)} \exp(2\pi i D z)]. \quad (6)$$

Their amplitudes,

$$A_0 = \psi^{(1)} \exp(2\pi i D z) + \psi^{(2)},$$

and

$$A_g = \psi^{(2)} - \psi^{(1)} \exp(2\pi i D z),$$

are, by Eqs. (4),

$$A_0 = \cos(\tfrac{1}{2}\alpha) \exp(i\varphi) - i\sin(\tfrac{1}{2}\alpha), \quad (7)$$

and

$$A_g = -i\sin(\tfrac{1}{2}\alpha) - \cos(\tfrac{1}{2}\alpha) \exp(i\varphi), \quad (8)$$

where $\varphi = 2\pi D z$. It is evident that when $0 \leqq \alpha \leqq \pi$, $|A_0|^2$ decreases as z initially increases from zero, whereas $|A_g|^2$ increases as z initially increases. The difference of sign of contrast of the first fringe in both the 0-waves and G-waves according to whether α is positive or negative should be most strongly evident with $|\boldsymbol{g}\cdot\boldsymbol{f}| = 1/4$. In Fig. 6, drawn for the case of $\boldsymbol{g}\cdot\boldsymbol{f} = +1/8$, $|A_g|^2$ is the square of the resultant of vectors OA and OB and can be seen to increase as φ increases from zero. A_0 is the resultant of OA and OC, and so $|A_0|^2$ behaves oppositely to $|A_g|^2$. The usual X-ray topographic experiment records $|A_g|^2$, but it would be possible to take direct-beam projection topographs [17] of the fault fringes produced close to the exit face of a crystal 1 mm thick, and hence to record $|A_0|^2$. Summarising the above findings for diffracted-beam projection topographs of exit-face outcrops of fault surfaces, the rule is: "the contrast of first fringe is positive when $\boldsymbol{g}\cdot\boldsymbol{f}$ is positive".

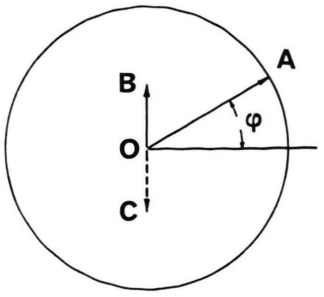

Fig. 6. Phase amplitude vector diagram drawn for $\boldsymbol{g}\cdot\boldsymbol{f} = \frac{1}{8}$, i. e. $\alpha = \pi/4$. Vector OA rotates anticlockwise as φ increases. Applications of diagram discussed in text.

Fault Surface Outcrop at Entrance Surface

It is questionable to apply plane-wave theory in the region near P, but in the present calculation which is only concerned with waves satisfying the Bragg angle exactly and which requires to know the phase difference between the branch (1) and the branch (2) waves as a function of depth below the entrance surface, it is adequate to express this difference as $\exp(2\pi i D z)$, provided that the origin of z is placed at a distance of about $(\frac{1}{4})\, D^{-1}$ above the entrance surface in Fig. 5, and attention is restricted to values of z not smaller than about $(\frac{3}{4})\, D^{-1}$. Provided also that z is not so great that the difference in attenuations of branch (1) and branch (2) waves traversing domain I need be considered, the wave-disturbance on the domain I side of the fault surface may be written as

$$\exp(-\pi i g x) + \exp(\pi i g x) + \exp(i\varphi)\,[\exp(-\pi i g x) - \exp(\pi i g x)]. \quad (9)$$

in which the phase factor $\exp(2\pi i k_z z)$ common to all terms is omitted and, as before, φ stands for $2\pi D z$. Expression (9) can be identified with the sum of branch (1) and branch (2) Bloch waves in domain II: this sum was given in expression (3). Substituting $x' = x - f_x$ and $\alpha = 2\pi \boldsymbol{g}\cdot\boldsymbol{f}$, the identifi-

cation of (9) with (3) gives

$$\psi^{(1)} = \cos(\alpha/2)\,\exp(i\varphi) - i\sin(\alpha/2)$$
and $$\psi^{(2)} = \cos(\alpha/2) - \sin(\alpha/2)\,\exp(i\varphi). \quad (10)$$

Now, according to assumptions (iii), only branch (1) waves need be considered after propagation from near P all the way to the exit surface. These waves emerge from the crystal as beams equal in intensity in both incident and diffracted directions. Thus $|A_0|^2$ and $|A_g|^2$ show similar contrast, and are proportional to $|\psi^{(1)}|^2$. Suppose $\boldsymbol{g}\cdot\boldsymbol{f} = +1/8$, as before. Then, with conditions equivalent to those shown in Fig. 6, both $|A_0|^2$ and $|A_g|^2$ are decreasing as z is increasing.

5. Comparison of Observations with Theory

The justification of the rudimentary theory just presented really rests upon its good agreement with experiment, at least as far as exit-surface outcrops are concerned. Early in 1966 the author recorded X-ray topographs of 40 different reflections from the specimen of which parts are shown in Figs. 3 and 4, and observed the contrast at the Brazil twin boundaries within it. These included two boundaries with composition planes of form r: $(10\bar{1}1)$ gently inclined to the specimen surface, and $(0\bar{1}11)$ steeply inclined thereto. From all this evidence on values of $|\boldsymbol{g}\cdot\boldsymbol{f}|$ the magnitude and orientation of $\boldsymbol{f}$ at each boundary could be determined with an accuracy of a few per cent. A boundary-structure model was devised which involved very little distortion of the normal bond lengths and angles. It requires a fault vector parallel to the $\boldsymbol{a}$-axis in the composition plane and of magnitude about $0.44\,a$. This vector produces values of $|\boldsymbol{g}\cdot\boldsymbol{f}|$ that account well for the observed boundary visibilities. (It is hoped to write an account of this work in due course.) Since the structural hand of domains I and II could be found from their optical rotations, the sign of $\boldsymbol{f}$ could also be predicted from the structure model. This agreed with the sign found from first-fringe contrast at the exit-face outcrop of the $(10\bar{1}1)$-orientation boundary on all $h\,h\,l$, $\bar{h}\,\bar{k}\,l$ pairs of topographs taken under not highly asymmetric transmission geometry, provided α was of apropriate magnitude and strong reflections, i. e. those for which ε is relatively high, were used. Even at the twin boundary parallel to $(0\bar{1}11)$, which made a steep angle with the specimen surface, the expected contrast reversal in $h\,k\,l$, $\bar{h}\,\bar{k}\,l$ pairs was observed at its exit surface outcrop in the appropriate reflections and when the projected image of the boundary was wide enough to allow clear observation of the first fringe.

Regarding twin boundary outcrops at the X-ray entrance surface, only one $h\,k\,l$, $\bar{h}\,\bar{k}\,l$ pair of topographs was taken with the usual X-ray entrance and exit surfaces reversed so as to make the $(10\bar{1}1)$-orientation boundary outcrop at the entrance surface. On the topograph in which excess intensity was predicted in the first fringe, strong excess was indeed observed. However, in the inverse reflection it appeared that the first maximum and first minimum were merged to give net weak excess intensity over the perfect-crystal background intensity. Thus only the *difference* in contrast in the $h\,k\,l$, $\bar{k}\,\bar{h}\,l$ pair was in the expected sense. On the twin boundaries steeply inclined to the specimen surface the image-spreading effects of X-ray propagation through the 1 mm crystal thickness prevented resolution of the small projected fringe spacing at the entrance-surface outcrop, so that differences of contrast between first-fringe images could not be discerned.

From the observations made it can be concluded that the assumptions (i) in Sect. 4 are not severely restricting upon the diffraction geometry under which sign determinations of α-boundary fault vectors can be performed by X-ray topography. The highly simplifying assumption (ii) is justified by experience with projection topographs of Pendellösung fringes taken at or near symmetrical Laue transmission geometry, as well as by comparison of section topograph and projection topograph images of α-boundaries. However, the whole analysis, as well as the particular assumption (ii), require that domains I and II are of essentially undeformed crystal. That is, there is no source of interbranch scattering other than the fault-surface itself, and in neither domain is there any significant energy-flow curvature [15] due to lattice-plane curvature. In Figs. 3 and 4 the contrast variations due to growth banding have a spacing small compared with the fault-fringe spacing and do not cause confusion. (This is not always the case. Very complex patterns can be generated when twin-boundaries and growth-bands produce fringe patterns of similar spacing, especially when the latter cause some interbranch scattering [18].) It is also essential that the transition region between domains I and II should contain no stressed material on such a scale as would produce

X-ray diffraction contrast because of lattice-plane curvature attendant upon stress relief where the fault surface outcrops at a free surface. This type of contrast, when present, easily masks the first-fringe contrast effects here considered. In fact, the author's model for Brazil twin boundaries on composition surfaces of form r is quite stress-free; and section topographs have confirmed that such boundaries are ideal, stress-free α-boundaries [18]. The present specimen had been roughly polished before X-ray examination, and thorough etching was necessary in order to remove all surface strains. The lines appearing on Figs. 3 and 4 which run from upper left to lower right and which make about 20° with the vertical are images of grooves in the surface where abrasion-damaged material has been etched away. The contrast produced by these grooves arises from the slopes of the sides of the grooves modifying the exit-surface boundary conditions so as to vary the partition of intensity between the incident-beam and diffracted-beam directions. It would have been desirable to repolish the specimen but such action would have involved undesirable loss of some of the $(10\bar{1}1)$ twin boundary surface. The ragged appearance of the outcrop trace of this boundary, which is particularly evident on Fig. 4 a, arises from the pitted and grooved character of the specimen surface.

Finally, consider assumption (iii) of Section 4. The ratio ε has rather similar values for both $10\bar{1}1$ and $20\bar{2}0$ reflections. Including an isotropic Debye-Waller factor but assuming that for both silicon and oxygen atoms f_g''/f_0'' is unity, ε is found to be 0.70 for the $10\bar{1}1$ reflection and 0.68 for the $20\bar{2}0$ reflection at room temperature. With symmetrical Laue case transmission of MoKα radiation through an unfaulted crystal 1 mm thick, and with waves exactly satisfying the Bragg condition in the crystal, the intensity dominance of branch (1) waves over branch (2) waves at the exit face is four-fold for the $10\bar{1}1$ reflection and is still more than three-fold for the π-polarisation state waves in the case of the $20\bar{2}0$ reflection. The conclusions drawn from the experiments are that assumptions (ii) and (iii) taken in conjunction form a valid basis for predicting fault-fringe contrast on X-ray projection topographs even with μt values as low as 1 provided ε is, say, not less than about 2/3. This may not be of much theoretical significance but it certainly has practical utility in the determination of the sign of fault vectors.

[1] A. R. LANG, Acta Cryst. **12**, 249 [1959].
[2] N. KATO and A. R. LANG, Acta Cryst. **12**, 789 [1959].
[3] N. KATO, Acta Cryst. **14**, 526, 627 [1961].
[4] N. KATO, in: Crystallography and Crystal Perfection, ed. G. N. RAMACHANDRAN, Academic Press, London, New York 1963, p. 153.
[5] P. B. HIRSCH, A. HOWIE, R. B. NICHOLSON, D. W. PASHLEY, and M. J. WHELAN, Electron Microscopy of Thin Crystals, Butterworths, London 1965.
[6] S. AMELINCKX, in: Modern Diffraction and Imaging Techniques in Material Science, ed. S. AMELINCKX, R. GEVERS, R. REMAUT, and J. VAN LANDUYT, North-Holland Publishing Co., Amsterdam 1970, p. 257.
[7] A. R. LANG, J. Phys. Chem. Solids, Suppl. No. 1, 833 [1967].
[8] A. R. LANG, in: Modern Diffraction and Imaging Techniques in Material Science, ed. S. AMELINCKX, R. GEVERS, G. REMAUT, and J. VAN LANDUYT, North-Holland Publishing Co., Amsterdam 1970, p. 407.
[9] R. GEVERS, J. VAN LANDUYT, and S. AMELINCKX, Phys. Stat. Sol. **11**, 689 [1965].
[10] S. MARDIX, A. R. LANG, and I. BLECH, Phil. Mag. **24**, 683 [1971].
[11] N. KATO, K. USAMI, and T. KATAGAWA, in: Advances in X-ray Analysis, Vol. 10, Plenum Press, New York 1967, p. 46.
[12] A. AUTHIER, Phys. Stat. Sol. **27**, 77 [1968].
[13] A. AUTHIER and M. SAUVAGE, J. Physique **27**, C3-137 [1966].
[14] A. R. LANG, Appl. Phys. Lett. **7**, 168 [1965].
[15] P. PENNING and D. POLDER, Philips Res. Rep. **16**, 419 [1961].
[16] H. HASHIMOTO, A. HOWIE, and M. J. WHELAN, Proc. Roy. Soc. London A **269**, 80 [1962].
[17] A. R. LANG, Brit. J. Appl. Phys. **14**, 904 [1963].
[18] A. R. LANG, in: Advances in X-ray Analysis, Vol. 10, Plenum Press, New York 1967, p. 91.